RSC Advances

PAPER

View Article Online
View Journal | View Issue

Cite this: *RSC Adv.*, 2018, **8**, 10954

Enhanced near infrared persistent luminescence of $Zn_2Ga_{2.98}Ge_{0.75}O_8:Cr_{0.02}^{3+}$ nanoparticles by partial substitution of Ge^{4+} by Sn^{4+}

Ting Song, Meng Zhang, Yuxue Liu,* Jian Yang, Zheng Gong, Hong Yan, Hancheng Zhu, Duanting Yan, Chunguang Liu and Changshan Xu

Received 2nd February 2018
Accepted 12th March 2018

DOI: 10.1039/c8ra01036f

rsc.li/rsc-advances

Spinel-phase $Zn_2Ga_{2.98}Ge_{0.75-x}Sn_xO_8:Cr_{0.02}^{3+}$ (ZGGSO:Cr^{3+}) nanoparticles with various Sn^{4+} concentrations were prepared by a hydrothermal method in combination with a post-annealing in vacuum at high temperature. For these nanoparticles, the observed near infrared (NIR) persistent luminescence peaked at ~697 nm and originates from the ^2E, $^4T_2$ (^4F) → $^4A_2$ transitions of Cr^{3+} and the afterglow time exceeds 800 min. For both the interior and surface Cr^{3+} ions in the ZGGSO host, it can be found that the increased energy transfer from Cr^{3+} to the deep trap (anti-site defects, $Ga_{Zn}^{0} - Zn'_{Ga}$) after the substitution of Ge^{4+} by Sn^{4+} plays a key role in enhancing the persistent luminescence of the ZGGSO:Cr^{3+} nanoparticles. Strikingly, this energy transfer process can be controlled through the variations in the crystal field strength and the trap depths. Our results suggest that not only Sn^{4+} substitution can improve *in vivo* bioimaging but also the existence of deep traps in ZGGSO:Cr^{3+} nanoparticles is helpful for retracing *in vivo* bioimaging at any time.

Introduction

Nowadays, the materials and techniques related to *in vivo* bioimaging have attracted increasing attention because of their unique advantages, such as high sensitivity, contrast, resolution and *in situ* imaging during detection and therapy.[1–8] Among them, the strategy adopting near infrared (NIR) persistent luminescence nanoparticles (PLNPs) is one of the most promising techniques because it does not need external excitation and possesses high penetrability during bioimaging.[9–19] In particular, Cr^{3+} doped zinc gallate (ZGO:Cr^{3+}) based PLNPs have been employed because its $3d^3$ electron configuration permits a narrow-band emission around 700 nm, which falls in the tissue optical window (650–1000 nm).[20–28]

To understand how to enhance the persistent luminescence of ZGO:Cr^{3+}, many efforts have been made by researchers. For example, Bessière *et al.* believed that, for Cr^{3+} doped $ZnGa_2O_4$ (ZGO:Cr^{3+}) powders with spinel structure, the NIR persistent emissions at ~695 nm originate from the distorted octahedral Cr^{3+} ions surrounded by anti-site pairs($Ga_{Zn}^{0} - Zn'_{Ga}$).[29–31] In particular, Pan *et al.* found that the NIR afterglow time of Cr^{3+} doped zinc gallogermanate ($Zn_3Ga_2Ge_2O_{10}$:0:5% Cr^{3+}) ceramics can be reached to more than 360 hours through the substitution of Ga^{3+} by Ge^{4+} due to the increased number of anti-sites defects.[32,33] Our previous study found that, for Cr^{3+} doped zinc gallogermanate ($Zn_2Ga_{2.98-x}Ge_{0.75}O_8:Cr_{0.020}$, Pr_x) nanoparticles, the substitution of Ga^{3+} by Pr^{3+} can simultaneously decrease the particle size and enhance the NIR persistent luminescence.[34] The related mechanism can be attributed to the generated anti-site defects and the suppressed energy transfer of the excited electrons from the $^4T_2$ level to the deep trap level related to anti-site pairs around the distorted octahedral Cr^{3+} ions.[31,34–37] However, for Cr^{3+} doped zinc gallogermanate nanoparticles, the effects of the variations in the crystal filed strength around Cr^{3+} ions and the depths of deep trap levels related to anti-sites on influencing the energy transfer from Cr^{3+} to the deep trap level still remain unclear.

Because cation substitution is an efficient approach to vary the crystal filed environments around luminescent centers, such as the bond length and crystal field strength, the substitution of Ge^{4+} by Sn^{4+} was employed in Cr^{3+} doped zinc gallogermanate nanoparticles.[38] Here, the compositions of the samples with various Sn^{4+} concentrations (x) can be represented as $Zn_2Ga_{2.98}Ge_{0.75-x}Sn_xO_8:Cr_{0.020}^{3+}$. Furthermore, it is also essential to understand how Sn^{4+} substitution and the deep trap affect the bioimaging applications. Thus, this study can give the comprehension of how to design new Cr^{3+} doped zinc gallogermanate nanoparticles for *in vivo* bioimaging.

In this work, spinel-phase ZGGSO:Cr^{3+} nanoparticles with various Sn^{4+} concentrations were prepared by a hydrothermal method in combination with a post-annealing in vacuum at 800 °C. The effects of Sn^{4+} substitution on bond lengths, crystal filed strength, trap depth and the energy transfer from Cr^{3+} to the deep traps were studied in detail. For these nanoparticles, the observed near infrared (NIR) persistent luminescence

School of Physics, Northeast Normal University, 5268 Renmin Street, Changchun, 130024, China. E-mail: yxliu@nenu.edu.cn

peaked at ~697 nm originates from the ^2E, $^4T_2$ (^4F) → $^4A_2$ transitions of Cr^{3+} and the afterglow time exceeds 800 min. For both the interior and surface Cr^{3+} ions in the ZGGSO host, it can be found that the increased energy transfer from Cr^{3+} to the deep trap (anti-site defects, $Ga^0_{Zn} - Zn'_{Ga}$) after the substitution of Ge^{4+} by Sn^{4+} plays a key role in enhancing the persistent luminescence of the ZGGSO:Cr^{3+} nanoparticles. Meanwhile, this energy transfer process can be controlled through the variations in the crystal field strength and the trap depths. Strikingly, our results suggest that an 808 nm stimulation is an efficient way to retrace *in vivo* bioimaging in the case that the persistent luminescence of NIR ZGGSO:Cr^{3+} nanoparticles is undetectable.

Synthesis and characterization

$Zn_2Ga_{2.98}Ge_{0.75-x}Sn_xO_8:Cr_{0.02}{}^{3+}$ (ZGGSO:Cr^{3+}) nanoparticles with various Sn^{4+} concentrations (x = 0, 0.015, 0.030, 0.063, 0.125 and 0.250) were prepared by a hydrothermal method in combination with a post-annealing in vacuum at high temperature. Gallium(III) nitrate hydrate ($Ga(NO_3)_3 \cdot xH_2O$, 99.9%) (Sigma-Aldrich), zinc acetate ($Zn(CH_3COO)_2$, 99.99%) (Aladdin), chromium(III) nitrate nonahydrate ($Cr(NO_3)_3 \cdot 9H_2O$, 99.95%) (Aladdin), tin(IV) chloride ($SnCl_4$, 99.99%) (Alfa Aesar) and germanium(IV) chloride ($GeCl_4$, 99.9999%) (Alfa Aesar) were used as starting materials. They were dissolved in deionized water according to the proposed metal mole ratio. Then the solution was transferred into a Teflon-line steel autoclave with a capacity of 40 ml and heated at 180 °C for 4 h in a drying oven. The generated precipitates were washed with deionized water three times and then dried at 80 °C for 6 h to obtain as-prepared ZGGSO:Cr^{3+} nanoparticles. The final nanoparticles were acquired by annealing the as-prepared nanoparticles at 800 °C in vacuum (pressure: 2.3×10^{-3} Pa) for 1.5 h.

The crystal structure of the samples was examined by a Rigaku D/MAX-2500 X-ray diffraction (XRD) spectrometer using Cu Kα radiation (0.15418 nm). The morphologies and compositions of the samples were characterized by means of a transmission electron microscope (TEM, JEOL-2100F). The Raman spectra were recorded by using a LabRAM HR Evolution Raman spectrometer (HORIBA) with a 488 nm excitation. The Rietveld refinements of XRD patterns were performed by GSAS program. The emission and excitation spectra, thermoluminescence (TL) and photostimulated luminescence (PSL) were recorded using a SHIMADZU RF-5301pc spectrophotometer equipped with a R928 photomultiplier tube. Especially, the emission spectrum at 80 K was obtained by using the above spectrophotometer in combination with INSTEC LN2-SYS Liquid Nitrogen Cooling Systems. The heating rate was 5 K min^{-1} and an 808 nm laser was used as a stimulation source. The afterglow decay curves were recorded by using a Zolix Omin λ-300 spectrophotometer. The measurements related to the luminescence kinetics of the samples were taken by an equipment combined with a LeCroy digital oscilloscope (62MXs-B), a Zolix Omin λ-300 spectrophotometer, an INNOLAS laser (SpitLight 600) and an INNOLAS optical parametric oscillator. X-ray photoelectron energy spectra (XPS) were obtained by using a Thermo ESCALAB 250 electron energy spectrometer with Al Kα radiation (1486.6 eV). All tests were performed at room temperature (RT) except for the TL measurements and part of emission spectra.

Results and discussion

Fig. 1a shows XRD patterns of $Zn_2Ga_{2.98}Ge_{0.75-x}Sn_xO_8:Cr_{0.02}{}^{3+}$ (ZGGSO:Cr^{3+}) powders with various Sn^{4+} concentrations (x = 0, 0.015, 0.030, 0.063, 0.125 and 0.250). For the samples with Sn^{4+} substitution concentrations ranging from 0 to 0.125, the diffraction peaks correspond well to those of the standard $ZnGa_2O_4$ sample (JCPDS: 38-1240). This result suggests that single phase $Zn_2Ga_{2.98}Ge_{0.75-x}Sn_xO_8:Cr_{0.02}{}^{3+}$ with spinel structure can be obtained. It can be explained by the replacement of Ga^{3+} by Ge^{4+}, Sn^{4+} and Cr^{3+} ions due to the fact that their ionic radii, Ge^{4+}(0.54 Å, CN = 6), Cr^{3+}(0.615 Å, CN = 6) and Sn^{4+}(0.69 Å, CN = 6), are similar to that of Ga^{3+}(0.62 Å, CN = 6).[39,40] Meanwhile, as the Sn^{4+} substitution concentration reaches to 0.250, additional XRD peaks related to impurity phases, such as Ga_2O_3, ZnO, GeO_2 and SnO_2 appear. It can be concluded that the maximum value of Sn^{4+} substitution concentration is lower than 0.250. In addition, for each sample with a certain Sn^{4+} concentration, the intensity ratio of (222) diffraction peak to (311) peak (I(222)/I(311)) was calculated and shown in Table 1. It can be found that the intensity ratios of the samples are in the range of 0.142–0.155, which is closer to that of $ZnGa_2O_4$ with normal spinel structure (0.13), but smaller than that of Zn_2GeO_4 with inversed spinel structure (0.20). This result indicates that the obtained samples maintain a normal spinel structure like $ZnGa_2O_4$.[40] In particular, a slight shift of the (311) peak to lower angles with an increase of Sn^{4+} substitution concentration can

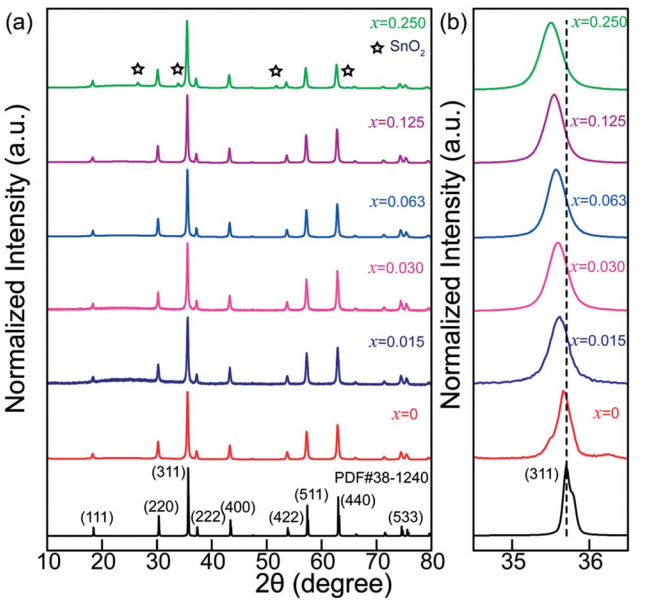

Fig. 1 (a) XRD patterns of ZGGSO:Cr^{3+} powders with various Sn^{4+} concentrations (x = 0, 0.015, 0.030, 0.063, 0.125 and 0.250). (b) The (311) peak position as a function of Sn^{4+} substitution concentration.

Table 1 The intensity ratio of (222) diffraction peak to (311) peak (I(222)/I(311)) and the size distribution of the ZGGSO:Cr^{3+} powders as a function of Sn^{4+} substitution concentration

Sample	I(222)/I(311)	Mean (nm)	Standard deviation (nm)
$x = 0$	0.144	37.7	6.4
$x = 0.015$	0.147	38.2	6.0
$x = 0.030$	0.151	38.0	5.9
$x = 0.063$	0.142	36.9	5.6
$x = 0.125$	0.147	37.5	7.5
$x = 0.250$	0.148	37.4	6.8

be observed, as shown in Fig. 1b, further proving that the crystal lattice spacing is increased due to the substitution of Ge^{4+} by Sn^{4+}.

To confirm the influence of Sn^{4+} substitution on the particle sizes of the samples, TEM images and EDS of ZGGSO:Cr^{3+} samples with various Sn^{4+} substitution concentrations (x = 0, 0.015, 0.030, 0.063, 0.125 and 0.250) are shown in Fig. 2a and b. It can be found that the average particle sizes of these samples are in the range 37.4–38.2 nm, as listed in Table 1. For all the samples, EDS signals related to Zn, Ga, Ge and O atoms in the ZGGO host can be observed. The signals related to Sn atom can be detected when the substitution concentration is equal to or larger than 0.063. The aforementioned results suggest that Sn^{4+} substitution has little influence on their particle sizes.

To further unravel the effect of Sn^{4+} substitution on the microstructure, the Rietveld refinements of XRD patterns for $Zn_2Ga_{2.98}Ge_{0.75-x}Sn_xO_8:Cr_{0.02}{}^{3+}$ nanoparticles with various Sn^{4+} substitution concentrations ranging from 0 to 0.125 are shown in Fig. 3. For each of the samples, the obtained goodness of fitting parameters, R_{wp}, R_p and χ^2, presented in Table 2, can ensure the reliability of the data fitting. Fig. 3b shows the calculated lattice constant, cell volume and Zn–O, Ga–O and Cr–O bond lengths as a function of Sn^{4+} substitution concentration. It can be found that these parameters increase with an increase of Sn^{4+} substitution concentrations because the ionic radius (0.62 Å) of Sn^{4+} is larger than that of Ge^{4+} (0.54 Å). In particular, the lattice constants and unit cell volumes show a slower increase as the Sn^{4+} substitution concentration is larger than 0.030. This suggests that it is difficult for Sn^{4+} ions substituting for interior Ge^{4+} ions and more Sn^{4+} ions appear on the surface of nanoparticles when x is larger than 0.030. This

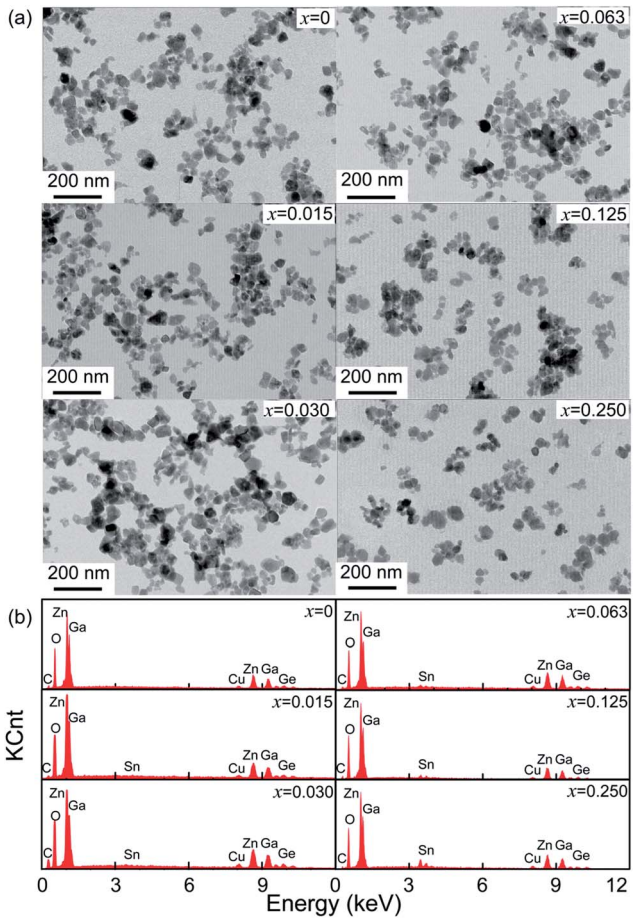

Fig. 2 (a) TEM images and (b) EDS of ZGGSO:Cr^{3+} nanoparticles with various Sn^{4+} concentrations (x = 0, 0.015, 0.030, 0.063, 0.125 and 0.250).

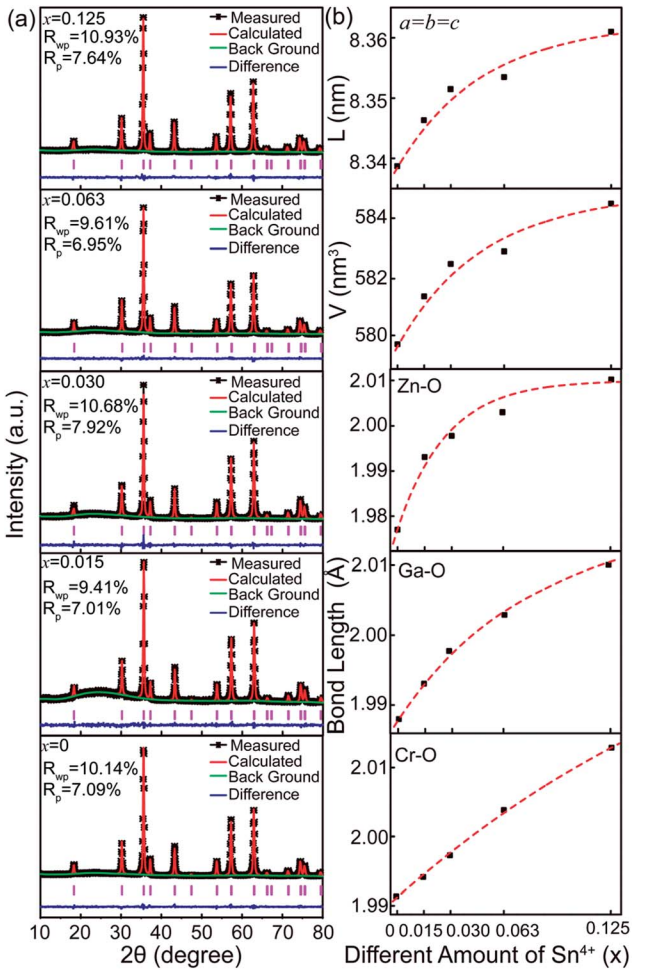

Fig. 3 (a) The Rietveld refinements of XRD data for ZGGSO:Cr^{3+} nanoparticles with various Sn^{4+} concentrations (x = 0, 0.015, 0.030, 0.063, 0.125 and 0.250). (b) The calculated lattice constant, cell volume and Zn–O, Ga–O and Cr–O bond lengths as a function of Sn^{4+} substitution concentration.

Table 2 The related fitting parameters for the Rietveld refinements of the XRD data as a function of Sn^{4+} substitution concentration

Sample	$x = 0$	$x = 0.015$	$x = 0.030$	$x = 0.063$	$x = 0.125$
R_{wp}	10.14%	9.41%	10.68%	9.61%	10.93%
R_p	7.09%	7.01%	7.92%	6.95%	7.64%
$a = b = c$ (nm)	8.339	8.347	8.34	8.351	8.361
$\alpha = \beta = \gamma$ (°)	90	90	90	90	90
Volume (nm^3)	579.941	581.547	581.940	582.557	584.477

result is consistent with the XRD data, showing that the diffraction peaks related to SnO_2 appear when x is equal to 0.250.

To illuminate the change in the microstructure induced by Sn^{4+} substitution, Fig. 4a and b show a cell of $ZnGa_2O_4$ with a spinel structure (AB_2X_4 formula) and Raman spectra of ZGGSO:Cr^{3+} nanoparticles with different Sn^{4+} substitution concentrations (x = 0, 0.015, 0.030, 0.063 and 0.125), respectively. In Fig. 4a, it can be found that a cell of ZGO contains a number of ZnO_4 tetrahedrons and GaO_6 octahedrons, which are centered by Zn^{2+} (occupying the A sites) and Ga^{3+} (occupying the B sites), respectively. On the basis of the study of Gorkom *et al.*, the allowed Raman modes, A_{1g}, E_g and T_{2g}, originating from the symmetric stretching vibrations of ZnO_4 groups can be found.[41] Therefore, in Fig. 4b, for each of the samples, it is reasonable to detect the obvious Raman peaks at around 720, 630 and 610 cm^{-1}, which are attributed to the A_{1g}, E_g and T_{2g} modes related to the Zn–O tetrahedron vibrations in the ZGGSO host, respectively.[34,42] This result further suggests that the ZGGSO:Cr^{3+} nanoparticles with normal spinel structure were obtained. In particular, the Raman peaks related to the A_{1g} mode show an obvious shift to lower wavenumbers with an increase of Sn^{4+} substitution concentration. This phenomenon might be explained by the increased Zn–O bond length due to partial substitution of Ge^{4+} by Sn^{4+}. For the Y_2O_3-stabilized ZrO_2 system, the similar result was reported by Hemberger *et al.*, who believed that the Raman band shift of the Zr–O stretching vibrations depends on the environments around the participating ions, such as Zr^{4+} ions, and the Raman band shift to lower frequencies is due to the increased Zr–O bond length with increasing Y_2O_3.[43] Because Sn^{4+} substitution also leads to the increased Cr–O and Ga–O bond lengths, it can be deduced that Sn^{4+} substitution might induce not only the change in the environments around Zn^{2+} ions, but also those around Cr^{3+} and Ga^{3+} ions.

To confirm the variation in the environments around Cr^{3+} ions induced by Sn^{4+} substitution, excitation and emission spectra of ZGGSO:Cr^{3+} with various Sn^{4+} substitution concentrations (x = 0, 0.015, 0.030, 0.063 and 0.125) are shown in Fig. 5a and b, respectively. For each of all the samples, it can be observed that each excitation spectrum contains several of absorption peaks ranging from 220 to 660 nm when the monitored wavelength is 697 nm. The obvious excitation peaks at around 250, 440 and 592 nm can be attributed to the charge transfer from O^{2-} to Cr^{3+}, the $^4A_2 \rightarrow {}^4T_1(^4F)$ and $^4A_2 \rightarrow {}^4T_2(^4F)$ transitions of Cr^{3+} ions, respectively. From room temperature emission spectra upon 592 nm excitation, it can be observed that there exist two emission peaks at 697 and 712 nm, respectively. On the basis of the previous study, they might be related to the transitions from the ^2E and $^4T_2$ (^4F) states to the $^4A_2$ state, respectively.[26,27,44,45] To better discern the NIR emissions from the ^2E and $^4T_2$ energy levels of Cr^{3+} ions doped in ZGGO nanoparticles, emission spectra at RT and 80 K are shown in the inset of Fig. 5b. For RT emission spectrum, it can be observed that there exists a narrow emission at ~697 nm superimposed on a broad emission band at ~712 nm. At 80 K, the contribution of the narrow emission to the emission spectrum becomes more dominating compared to the broad emission band. The above result is in agreement with the study reported by Chen *et al.*, who believed that the narrow emission at ~697 nm and the broad emission band at ~712 nm originated from the $E(^2G) \rightarrow {}^4A_2$ and $^4T_2$ (^4F) $\rightarrow {}^4A_2$ transitions, respectively.[46] In particular, Chen *et al.* found that the appearance of a narrow emission band superimposed on the broad emission band suggested that the Cr^{3+} ions were located in an intermediate crystal-field environment and the crystal field

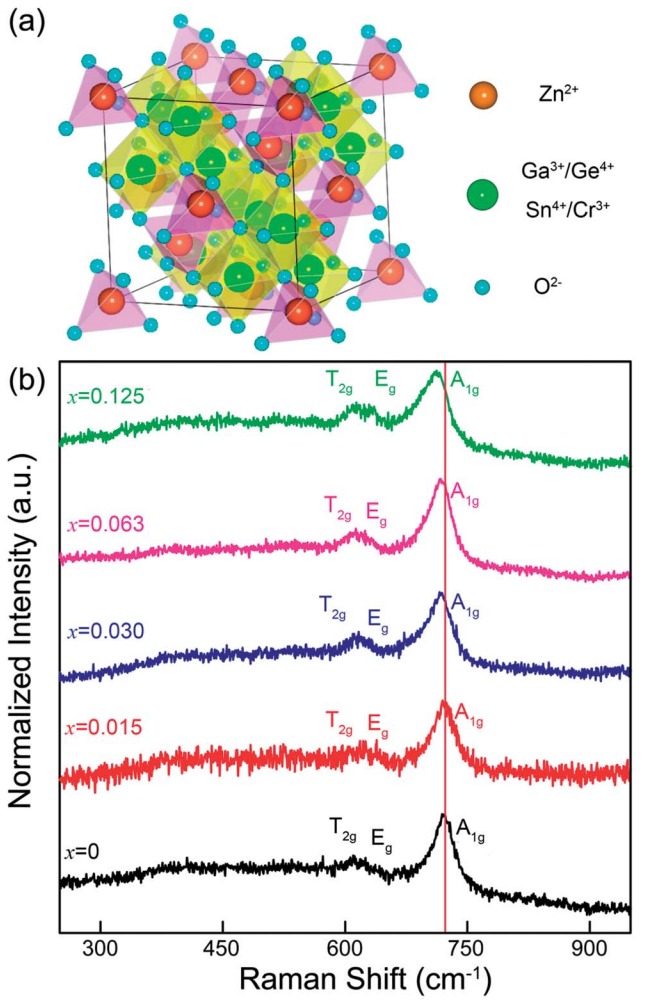

Fig. 4 (a) A cell of $ZnGa_2O_4$ with a spinel structure (AB_2X_4 formula). (b) Raman spectra of ZGGSO:Cr^{3+} nanoparticles with different Sn^{4+} substitution concentrations (x = 0, 0.015, 0.030, 0.063 and 0.125).

strength is close to the crossing between the $^4T_2$ (^4F) and ^2E levels as shown in Fig. 5c.[46,47] To further prove the above conclusion, Fig. 5d shows normalized emission spectra recorded at RT of ZGGSO:Cr^{3+} nanoparticles with various Sn^{4+} concentrations upon 592 nm excitation. From the enlarged part, it can be found that the intensity ratio of the 712 nm emission peak to the 697 nm emission peak increases with increasing Sn^{4+} substitution concentration. Our result is similar to that reported by Chen *et al.*, who found that, for Cr^{3+} doped $Bi_2(Ga/Al)_4O_9$, the substitution of Al^{3+} for Ga^{3+} could lead to the decreased ratio of broadband emission to the narrow emission and the stronger crystal field strength around Cr^{3+} ions.[48] In our case, it can be deduced that Sn^{4+} substitution will give rise to the weakened crystal field strength around Cr^{3+} ions. Furthermore, on the basis of the study reported by Hermus *et al.*, the relationship between the crystal field strength (D_q) around the luminescence center and the distance between the central atom (Cr^{3+}) and the ligand (O^{2-}) (R) can be expressed in the following equation:[49]

$$D_q = \frac{Ze^2r^4}{6R^5} \quad (1)$$

where Z and e are the charges of the anion and electron, respectively, and r is the radius of the 3d wave functions. It can be found that the increased R value, namely, the increased Cr–O bond length, induced by Sn^{4+} substitution, gives rise to the weakened crystal filed strength, D_q. Thus, for ZGGSO:Cr^{3+} nanoparticles, it is possible that Sn^{4+} substitution will lead to the weakened strength of crystal field around Cr^{3+} ions and the enhanced transition from the $^4T_2$ state to the $^4A_2$ state (emission located at 712 nm).

To understand how Sn^{4+} substitution influences the persistent luminescence of nanoparticles, afterglow decay curves of ZGGSO:Cr^{3+} nanoparticles with various Sn^{4+} substitution concentrations ($x = 0$, 0.015, 0.030, 0.063 and 0.125) monitored at 697 nm are shown in Fig. 6. For each of the samples, it can be found that the afterglow time exceeds 800 min (>13 h). This result is consistent with the fact that the obvious phosphorescence at 812 min after the stoppage of 254 nm irradiation can be detected as shown in the inset of Fig. 6. In particular, the afterglow intensities show an initial rise and a subsequent decrease with increasing Sn^{4+} substitution concentration from 0 to 0.125. The strongest afterglow intensity of the ZGGSO:Cr^{3+} nanoparticles with $x = 0.015$ can be obtained and its intensity recorded at 60 min after stopping 254 nm irradiation is ~1.7 times as strong as that of the ZGGO:Cr^{3+} nanoparticles ($x = 0$). This result suggests that Sn^{4+} substitution can enhance the afterglow intensity of ZGGO:Cr^{3+} nanoparticles. According to our previous study on Pr^{3+} doped ZGGO:Cr^{3+} nanoparticles,[50,51] the enhanced persistent luminescence can be explained by the increased number of the distorted Cr^{3+} ions and more generated anti-site defects around them due to Sn^{4+} substitution.[38,52]

To unravel the effect of Sn^{4+} substitution on the depth of the traps, TL spectra of ZGGSO:Cr^{3+} nanoparticles with various Sn^{4+} concentrations ($x = 0$, 0.015, 0.030, 0.063 and 0.125) are shown in Fig. 7. For each of all TL spectra, it can be observed that there exists a single broad TL peak at around 350 K. In particular, the TL peak position shifts to lower temperatures with increasing

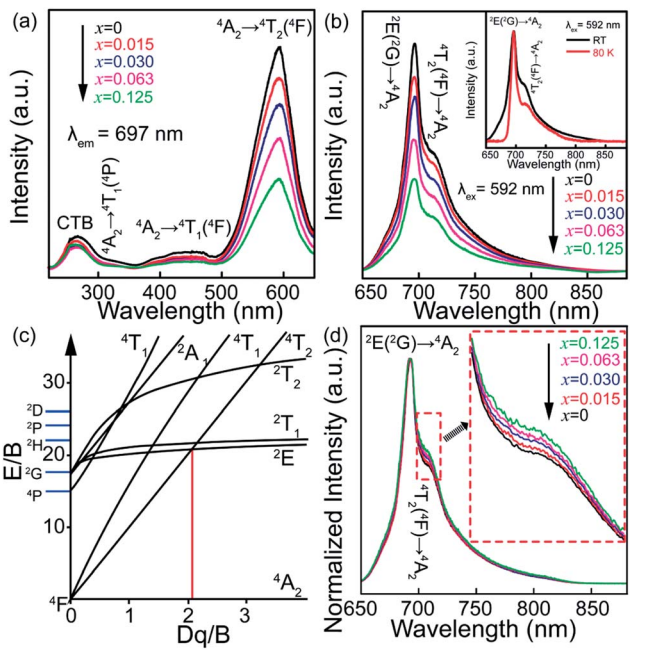

Fig. 5 (a) Excitation (λ_{em} = 697 nm) and (b) emission (λ_{em} = 592 nm) spectra at RT of ZGGSO:Cr^{3+} nanoparticles with various Sn^{4+} substitution concentrations ($x = 0$, 0.015, 0.030, 0.063 and 0.125). The inset gives the emission spectra of ZGGSO:Cr^{3+} without Sn^{4+} at RT and 80 K, respectively. (c) Tanabe–Sugano diagram for Cr^{3+} ion in an octahedral site. The position of the intermediate crystal field strength (D_q/B = ~2.3) is marked by the red solid line. (d) The normalized emission spectra recorded at RT. The inset gives the enlarged region.

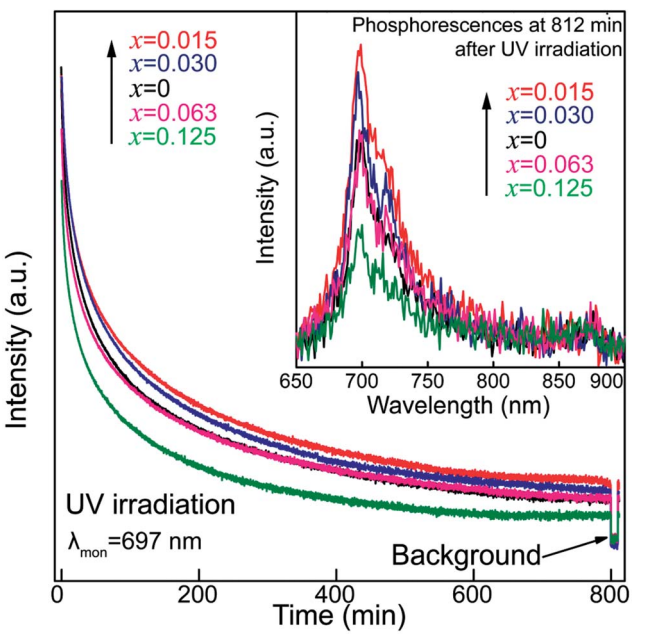

Fig. 6 The afterglow decay curves of ZGGSO:Cr^{3+} nanoparticles with various Sn^{4+} substitution concentrations ($x = 0$, 0.015, 0.030, 0.063 and 0.125) upon 254 nm excitation. The inset shows their phosphorescence spectra.

Sn^{4+} concentration. Generally, the trap depths can be obtained through the following equation:

$$E_t = T_m/500 \quad (2)$$

where E_t is the calculated trap depth and T_m is the temperature corresponding to the TL peak position. It can be found that the E_t value decreases from 0.72 to 0.68 eV with increasing Sn^{4+} substitution amounts. It can be concluded that the trap depths are altered through Sn^{4+} substitution.[53] Based on the study reported by Bessière *et al.*, the traps with a depth of ~0.7 eV can be attributed to the contribution of anti-site defects ($Ga^{0}_{Zn} - Zn'_{Ga}$) around distorted Cr^{3+} ions.[31] According to our previous study on Pr^{3+} doped ZGGO:Cr^{3+} nanoparticles, the decrease of trap depth with increasing Sn^{4+} concentration indicates that anti-site defects are closer to distorted Cr^{3+} ions due to the increased numbers of the generated anti-site defects and distorted Cr^{3+} ions after Sn^{4+} substitution.[34]

To further understand how Sn^{4+} substitution affects the surface distributions of Zn^{2+} and Ga^{3+} ions, XPS spectra of Zn $2p_{3/2}$ and Ga $3d_{5/2}$ core levels for ZGGSO:Cr^{3+} nanoparticles with various Sn^{4+} concentrations (x = 0, 0.015, 0.030, 0.063 and 0.125) are shown in Fig. 8a and b. These XPS peaks were calibrated by using the C 1s peak at 284.6 eV. For each of the samples with various Sn^{4+} concentrations, the binding energies of the Zn $2p_{3/2}$ and Ga $3d_{5/2}$ core levels can be obtained by fitting with a single Gaussian function, as listed in Table 3. On the basis of the afterglow spectral analysis and our previous XPS study on Pr^{3+} doped ZGGO:Cr^{3+} nanoparticles, it can be inferred that there merely exist Zn^{2+} ions in the tetrahedral sites and Ga^{3+} ions in the octahedral sites on the surface of the ZGGSO:Cr^{3+} nanoparticles, suggesting that Sn^{4+} substitution mainly leads to the generation of anti-site defects in the interior of the ZGGSO:Cr^{3+} nanoparticles.[34] Strikingly, the peak positions related to the Zn $2p_{3/2}$ and Ga $3d_{5/2}$ core levels exhibit an initial decrease and a following increase with increasing Sn^{4+} concentration. The decreased binding energies of the Zn $2p_{3/2}$ and Ga $3d_{5/2}$ core levels with a rise of Sn^{4+} concentration might be related to the increased Zn–O and Ga–O bond lengths due to Sn^{4+} substitution. For carbon nitride systems, the similar behavior were also reported by Titantah *et al.*, who found that the N 1s binding energy decreases with increasing C–N bond length.[54] Meanwhile, the increased Zn $2p_{3/2}$ and Ga $3d_{5/2}$ binding energies can be attributed to the deformations of ZnO_4

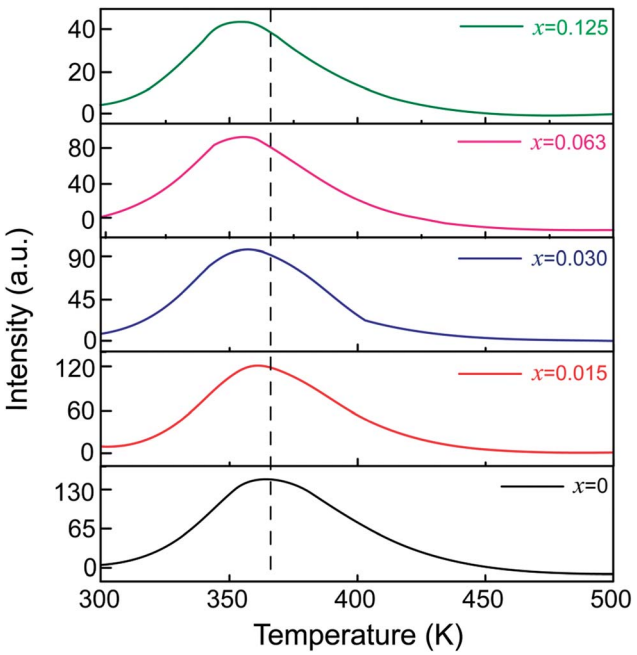

Fig. 7 TL spectra of ZGGSO:Cr^{3+} nanoparticles with various Sn^{4+} concentrations (x = 0, 0.015, 0.030, 0.063 and 0.125).

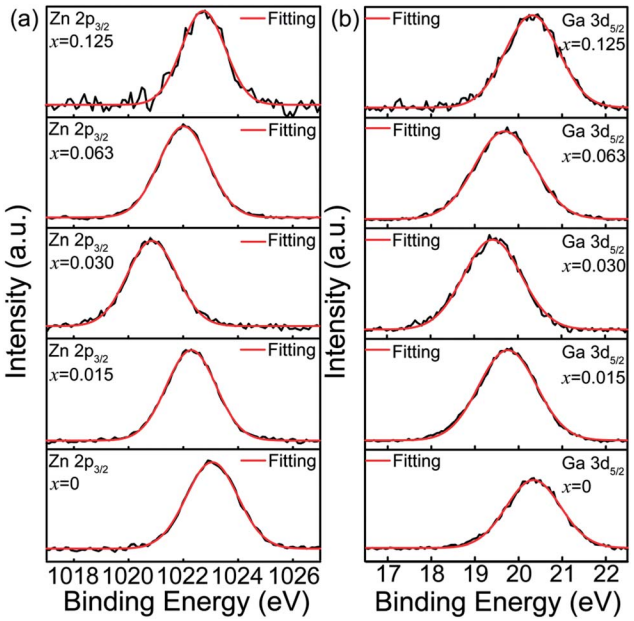

Fig. 8 XPS spectra of (a) Zn $2p_{3/2}$ and (b) Ga $3d_{5/2}$ core levels for ZGGSO:Cr^{3+} nanoparticles with various Sn^{4+} concentrations (x = 0, 0.015, 0.030, 0.063 and 0.125).

Table 3 The binding energies of the Zn $2p_{3/2}$ and Ga $3d_{5/2}$ core levels and the related lifetimes of the ZGGSO:Cr^{3+} nanoparticles with various Sn^{4+} substitution concentrations[a]

	Zn $2p_{3/2}$	Ga $3d_{5/2}$	Decay ($^4T_2 \rightarrow {}^4A_2$)[d]		Decay ($^2E \rightarrow {}^4A_2$)[e]	
x	BE (eV)[b]	BE (eV)[c]	τ_s (μs)	τ_i (μs)	τ_s (ms)	τ_i (ms)
0	1023.1	20.3	78	668	2.23	6.63
0.015	1022.3	19.8	17	249	2.24	6.88
0.030	1020.9	19.4	19	218	2.62	7.43
0.063	1022.0	19.7	32	257	2.12	6.75
0.125	1022.7	20.3	34	398	2.06	6.71

[a] The samples are ZGGSO:Cr^{3+} with various Sn^{4+} concentrations (x = 0, 0.015, 0.030, 0.063, 0.125). [b] BE refers to the binding energies of the Zn $2p_{3/2}$ core level. [c] BE refers to the binding energies of the Ga $3d_{5/2}$ core level. [d] Emission decay of the $^4T_2 \rightarrow {}^4A_2$ transition. [e] Emission decay of the $^2E \rightarrow {}^4A_2$ transition. τ_s and τ_i represent the lifetimes related to the surface and interior Cr^{3+} ions, respectively.

tetrahedrons and GaO_6 octahedrons after Sn^{4+} substitution based on our previous study on Pr^{3+} doped ZGGO:Cr^{3+} nanoparticles.[34]

To further illuminate the effect of Sn^{4+} substitution on the surroundings of Cr^{3+} ions, the decay curves of the 697 nm emission of ZGGSO:Cr^{3+} nanoparticles with various Sn^{4+} concentrations (x = 0, 0.015, 0.030, 0.063 and 0.125) under 575 nm excitation are shown in Fig. 9. In analogy with our previous study on Pr^{3+} doped ZGGO:Cr^{3+} nanoparticles, for each of the samples with various Sn^{4+} concentrations, the fitted lifetimes, as listed in Table 3, consist of four components.[34] Herein, for ZGGSO:Cr^{3+} nanoparticles, all of the decay curves need to be fitted with a sum of four exponentials. The two longer lifetimes (unit: ms) are related to the $^2E(^2G) \rightarrow {}^4A_2$ transitions of Cr^{3+} due to the forbidden spin-selection rule. The two shorter lifetimes (unit: μs) are related to the allowed $^4T_2$ (^4F) $\rightarrow {}^4A_2$ transitions of Cr^{3+}. Furthermore, Cr^{3+} ions doped in nanoparticles can be sorted into two different surroundings: surface and interior. The lifetime of the surface Cr^{3+} exhibits a shorter decay time because of Cr^{3+} occupying low-symmetry sites.[40]

Because the energy level position of the $^4T_2$ state is sensitive to the variation in the surroundings of Cr^{3+} ions (linearly depends on the variation in the crystal field strength), we focus on the effect of Sn^{4+} substitution on the lifetimes related to the $^4T_2 \rightarrow {}^4A_2$ emissions of the surface and interior Cr^{3+}. For both the surface and interior Cr^{3+} ions, it can be found that the lifetimes of Sn^{4+} doped nanoparticles are shorter than those of the undoped nanoparticles. Usually, the reciprocal of a lifetime (τ) can be expressed using a sum of radiative (W_R), nonradiative (W_{NR}) and energy transfer (W_{ET}) rates as follows:[34,55]

$$1/\tau = W_R + W_{NR} + W_{ET} \quad (3)$$

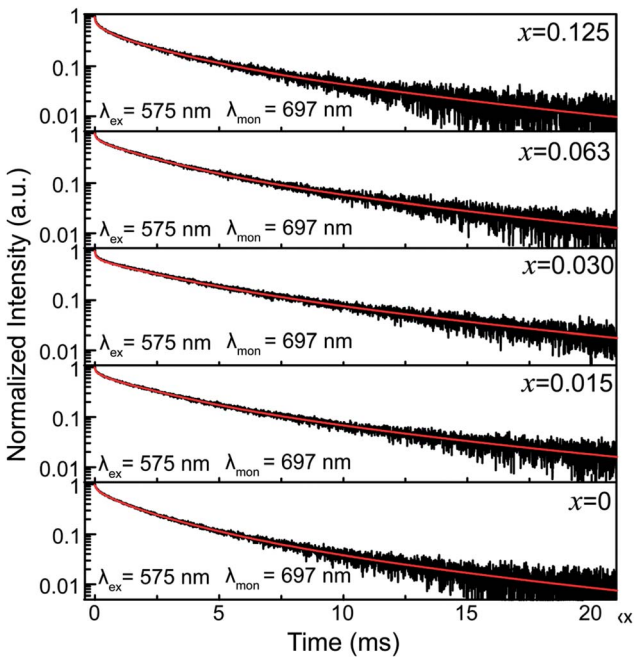

Fig. 9 The decay curves of ZGGSO:Cr^{3+} nanoparticles with various Sn^{4+} concentrations (x = 0, 0.015, 0.030, 0.063 and 0.125) monitored at 697 nm under 575 nm excitation.

It is known that the W_R value depends on the variation in the symmetry of the occupied sites and the W_{NR} value can be tuned by the variations of the particle size and phonon energy of the host after cation substitution. Based on the TEM observations and Raman, emission and absorption spectral analyses, it can be found that Sn^{4+} substitution leads to little variation in the W_R and W_{NR} values. Thus, in our case, the obtained lifetimes can be mainly ascribed to the contribution of the variation in the energy transfer rate after Sn^{4+} substitution. Since the emission intensity decreases with increasing Sn^{4+} concentration from Fig. 5b, it can be inferred that Sn^{4+} substitution gives rise to the increased energy transfer rate and the decreased lifetimes.

In addition, for both the surface and interior Cr^{3+} ions in the ZGGSO:Cr^{3+} nanoparticles with various Sn^{4+} concentrations, the corresponding lifetimes show an initial decrease and a following rise with increasing Sn^{4+} concentration. These phenomena might be explained by the variations in the $^4T_2$ level position of Cr^{3+} and the related trap depths after Sn^{4+} substitution. A schematic configuration coordinate diagram related to the energy transfer from Cr^{3+} to the deep traps under the $^4A_2$–$^4T_2$ excitation is given in Fig. 10 based on our previous studies.[34,40] Here, the deep traps refer to the anti-site pair ($Ga^0_{Zn} - Zn'_{Ga}$), which is close to the distorted Cr^{3+} ions, and the trap depths can be tuned by varying the distance between the anti-site pair and the distorted Cr^{3+} ion.[40] This distance will decrease with increasing the numbers of anti-site defects and distorted Cr^{3+} ions.[34] Because the numbers of the anti-site defects show an initial rise and a following decrease with increasing Sn^{4+} concentration, the distances between the anti-site pair and the distorted Cr^{3+} ions will initially decrease and then increase with increasing Sn^{4+} concentration. Thus, the variation in the deep trap depth will show a non-monotonic changing behaviour with increasing Sn^{4+} concentration. Meanwhile, Sn^{4+} substitution leads to the monotonously increased crystal field strength and the lowered bottom of the $^4T_2$ parabola. It can be deduced that Sn^{4+} substitution will cause the non-monotonic variations in the energy difference between the $^4T_2$ level and the deep traps related to the anti-site defects. Thus, the energy transfer from Cr^{3+} to the deep trap and the related lifetimes can be tuned through Sn^{4+} substitution. In particular, the sample (x = 0.015) with the shortest lifetimes corresponds to that with the strongest afterglow intensity, further indicating that the increased energy transfer from Cr^{3+} to the deep trap after Sn^{4+} substitution plays a key role in enhancing the persistent luminescence of the ZGGSO:Cr^{3+} nanoparticles. To prove the existence of the tunnelling mechanism, the afterglow decay curves of ZGGSO:Cr^{3+} nanoparticles without and containing Sn^{4+} (x = 0, 0.015) under 575 nm excitation are shown in Fig. 10b. For both of the samples, the strong persistent luminescence can be detected under visible light excitation. Strikingly, the afterglow intensity of the ZGGSO:Cr^{3+} containing Sn^{4+} (x = 0.015) is higher than that without Sn^{4+}. This result further suggests that Sn^{4+} substitution can enhance the persistent luminescence through controlling the tunnelling process. The detailed explanation is given as follows. For the excited electrons in the $^4T_2$ level upon 575 nm excitation, the tunnelling process will happen in the case that the bottom of

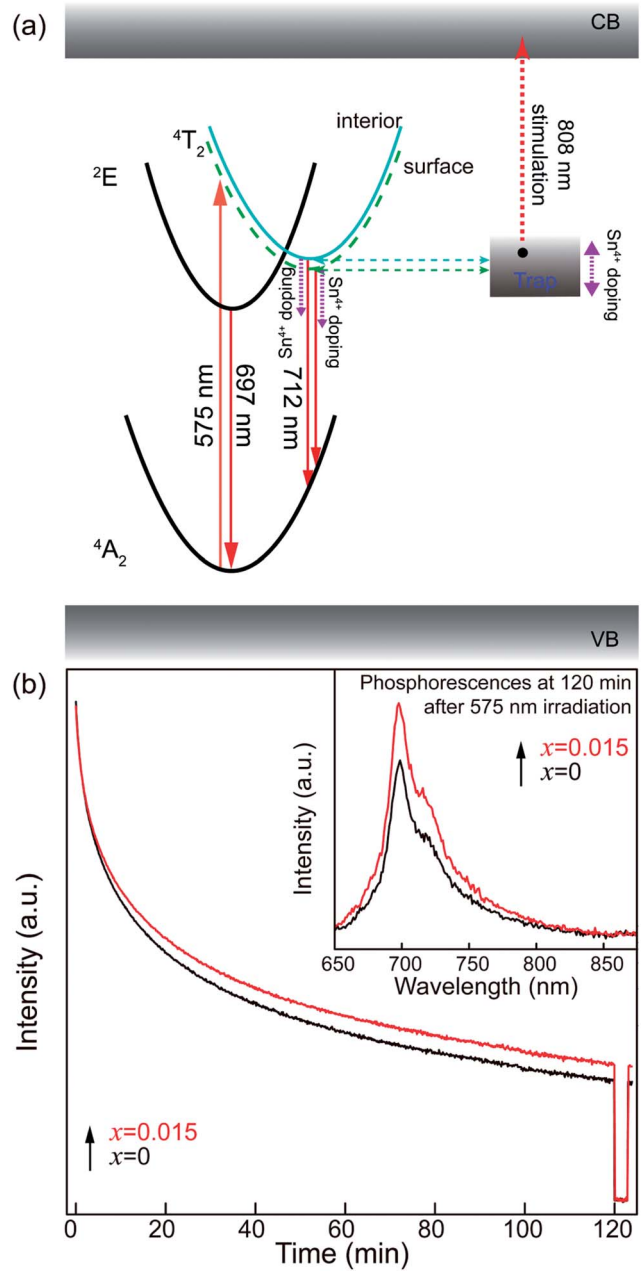

Fig. 10 (a) A schematic configuration coordinate diagram related to the energy transfer from Cr^{3+} ion to the deep traps under the $^4A_2$–$^4T_2$ excitation. (b) The afterglow decay curves of ZGGSO:Cr^{3+} nanoparticles without and containing Sn^{4+} (x = 0, 0.015) upon 575 nm excitation. The inset shows their phosphorescence spectra.

the $^4T_2$ parabola is far from the bottom of the conduction band of the host. Fortunately, for Cr^{3+} doped ZGO or ZGGO, it can be found that the $^4T_2$ level of Cr^{3+} is ~1.6–1.8 eV below the bottom of conduction band of the host based on the reported studies.[33,34,56] Thus, the observed persistent luminescence of ZGGSO:Cr^{3+} nanoparticles under 575 nm irradiation may originate from the tunnelling process between the $^4T_2$ and the deep traps.

To confirm the existence of the aforementioned deep traps in the ZGGSO nanoparticles, PSL spectra of ZGGSO:Cr^{3+} nanoparticles with various Sn^{4+} concentrations monitored at 697 nm (stimulation wavelength: 808 nm) after the stoppage of 254 nm irradiation for 5 min are shown in Fig. 11. Here, in order to realize high-quality *in vivo* bioimaging, we employed the 808 nm laser in the PSL measurement. For each of the samples, it can be found that a strong PSL signal superimposes on the afterglow curve when the 808 nm laser is on (the electrons stored in the deep traps are released). In particular, among ZGGSO:Cr^{3+} nanoparticles with various Sn^{4+} concentrations, the sample with $x = 0.015$ shows the strongest NIR luminescence, further proving that Sn^{4+} substitution can enhance the NIR persistent luminescence *via* tuning the energy transfer from Cr^{3+} to the deep traps. Meanwhile, at 30 min after stopping 254 nm irradiation, the PSL intensity is ~12 times as strong as the afterglow intensity without 808 nm stimulation. This result suggests that the strong NIR luminescence can be acquired using an 808 nm stimulation strategy in the case that the weak NIR afterglow intensity cannot be detected.

To demonstrate the effects of Sn^{4+} substitution and 808 nm stimulation on the bioimaging using NIR persistent luminescence nanoparticles, images of two pellets, pressed by the ZGGSO:Cr^{3+} nanoparticles without Sn^{4+} ($x = 0$) and containing Sn^{4+} ($x = 0.015$) upon 254 nm irradiation and 808 nm stimulation are shown in Fig. 12. The clear images of the two pellets were recorded using a digital camera under white light illumination, as shown in Fig. 12a. As the two pellets were taken at 1 min after stopping 254 nm irradiation, two red images can be observed, as shown in Fig. 12b. Strikingly, the image of the pellet containing Sn^{4+} is brighter than that without Sn^{4+}. This result is consistent with the afterglow spectral analysis. While, taken at 15 min or later after stopping 254 nm irradiation, the two red images become less clear, as shown in Fig. 12c and d. To retrace bioimaging in the case that the afterglow intensity is

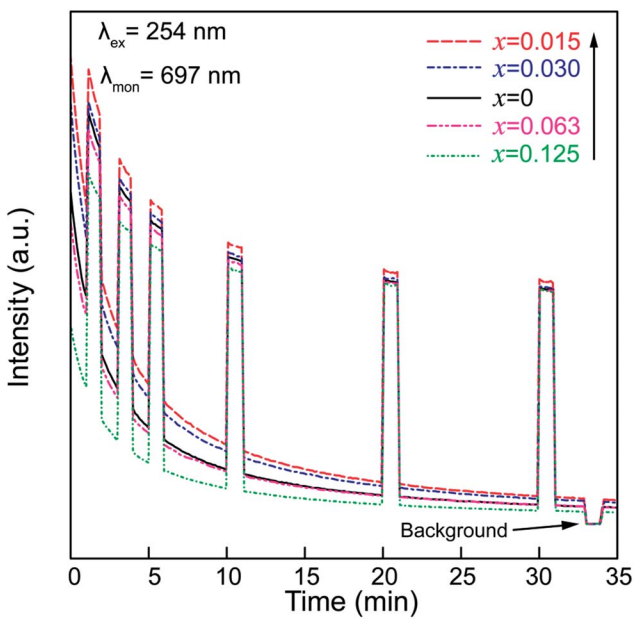

Fig. 11 PSL spectra of ZGGSO:Cr^{3+} nanoparticles with various Sn^{4+} concentrations monitored at 697 nm (stimulation wavelength: 808 nm) after the stoppage of 254 nm irradiation.

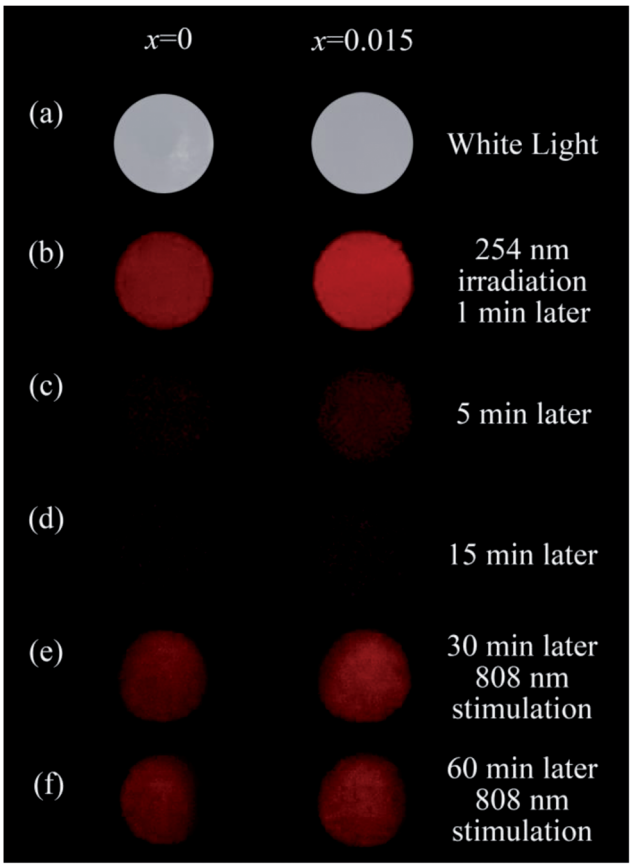

Fig. 12 (a) The photos of two pellets without Sn^{4+} and containing Sn^{4+} under white light illumination. (b–d) The NIR images of the two pellets without Sn^{4+} and containing Sn^{4+} were taken at 1, 5 and 15 min after stopping 254 irradiation. (e and f) The NIR images of the two pellets without Sn^{4+} and containing Sn^{4+}, originating from the NIR PSL stimulated by an 808 nm laser, taken at 30 and 60 min after stopping 254 nm irradiation.

undetectable, the images of the two pellets taken at 30 and 60 min after stopping 254 nm irradiation stimulated by an 808 nm laser are shown in Fig. 12e and f. It can be found that the two clear images, originating from the NIR PSL of ZGGSO:Cr^{3+} nanoparticles, reappear and the image of the pellet containing Sn^{4+} is still brighter than that without Sn^{4+}. This result suggests that 808 nm stimulation is an efficient way to retrace the bioimaging using NIR persistent luminescence nanoparticles. In addition, the power density of 808 nm excitation is ~7.8 mW cm^{-2}, which is much smaller than the critical value of photodamaged skin of human beings (330 mW cm^{-2}). This further can ensure the accuracy and security of *in vivo* bioimaging using ZGGSO:Cr^{3+} NIR PLNPs at any time.[57,58] Our results suggest that ZGGSO:Cr^{3+} nanoparticles have potential applications in *in vivo* bioimaging.

Conclusions

Spinel-phase ZGGSO:Cr^{3+} nanoparticles with various Sn^{4+} concentrations were prepared by a hydrothermal method in combination with a post-annealing in vacuum at 800 °C. It can be found that Sn^{4+} substitution has little influence on their particle sizes and leads to the increased Zn–O, Ga–O and Cr–O bond lengths. For these nanoparticles, the observed near infrared (NIR) persistent luminescence peaked at ~697 nm originates from the ^2E, $^4T_2$ (^4F) → $^4A_2$ transitions of Cr^{3+} and the afterglow time exceeds 800 min. For both the interior and surface Cr^{3+} ions in the ZGGSO host, it can be found that the increased energy transfer from Cr^{3+} to the deep trap (anti-site defects, $Ga^0_{Zn} - Zn'_{Ga}$) after the substitution of Ge^{4+} by Sn^{4+} plays a key role in enhancing the persistent luminescence of the ZGGSO:Cr^{3+} nanoparticles. It can be found that this energy transfer process can be controlled through the variations in the crystal field strength and the trap depths. Strikingly, our results suggest that not only Sn^{4+} substitution can improve *in vivo* bioimaging but also the existence of deep traps in ZGGSO:Cr^{3+} nanoparticles is helpful for retracing *in vivo* bioimaging at any time.

Conflicts of interest

There are no conflicts to declare.

Acknowledgements

This work was supported by the National Natural Science Foundation of China (no. 11674050, 11374047 & 11604044).

Notes and references

1 N. Basavaraju, K. R. Priolkar, A. Bessière, S. K. Sharma, D. Gourier, L. Binet, B. Viana and S. Emura, *Phys. Chem. Chem. Phys.*, 2017, **19**, 1369–1377.
2 T. Maldiney, A. Bessière, J. Seguin, E. Teston, S. K. Sharma, B. Viana, A. J. Bos, P. Dorenbos, M. Bessodes and D. Gourier, *Nat. Mater.*, 2014, **13**, 418.
3 S. Kidd, E. Spaeth, J. L. Dembinski, M. Dietrich, K. Watson, A. Klopp, V. L. Battula, M. Weil, M. Andreeff and F. C. Marini, *J. Stem Cells*, 2009, **27**, 2614–2623.
4 D. W. Bartlett, H. Su, I. J. Hildebrandt, W. A. Weber and M. E. Davis, *Proc. Natl. Acad. Sci. U. S. A.*, 2007, **104**, 15549–15554.
5 M.-K. So, C. Xu, A. M. Loening, S. S. Gambhir and J. Rao, *Nat. Biotechnol.*, 2006, **24**, 339.
6 A. Sato, B. Klaunberg and R. Tolwani, *Comp. Med.*, 2004, **54**, 631–634.
7 B. W. Rice, M. D. Cable and M. B. Nelson, *J. Biomed. Opt.*, 2001, **6**, 432–440.
8 J. Wang, J. Ye, H. Jiang, S. Gao, W. Ge, Y. Chen, C. Liu, C. Amatore and X. Wang, *RSC Adv.*, 2014, **4**, 37790–37795.
9 C. Rosticher, B. Viana, M. A. Fortin, J. Lagueux, L. Faucher and C. Chaneac, *RSC Adv.*, 2016, **6**, 55472–55478.
10 A. Mondal, S. Das and J. Manam, *RSC Adv.*, 2016, **6**, 82484–82495.
11 E. Teston, Y. Lalatonne, D. Elgrabli, G. Autret, L. Motte, F. Gazeau, D. Scherman, O. Clément, C. Richard and T. Maldiney, *Small*, 2015, **11**, 2696–2704.
12 Z. Li, Y. Zhang, X. Wu, L. Huang, D. Li, W. Fan and G. Han, *J. Am. Chem. Soc.*, 2015, **137**, 5304–5307.

13 Y.-C. Lu, C.-X. Yang and X.-P. Yan, *Nanoscale*, 2015, **7**, 17929–17937.
14 Y. Li, Y. Li, R. Chen, K. Sharafudeen, S. Zhou, M. Gecevicius, H. Wang, G. Dong, Y. Wu and X. Qin, *NPG Asia Mater.*, 2015, **7**, e180.
15 S. Singh, *RSC Adv.*, 2014, **4**, 58674–58698.
16 T. Maldiney, A. Lecointre, B. Viana, A. l. Bessieère, M. Bessodes, D. Gourier, C. Richard and D. Scherman, *J. Am. Chem. Soc.*, 2011, **133**, 11810–11815.
17 Q. l. M. de Chermont, C. Chanéac, J. Seguin, F. Pellé, S. Maîtrejean, J.-P. Jolivet, D. Gourier, M. Bessodes and D. Scherman, *Proc. Natl. Acad. Sci. U. S. A.*, 2007, **104**, 9266–9271.
18 W. Chen and J. Zhang, *J. Nanosci. Nanotechnol.*, 2006, **6**, 1159–1166.
19 R. Zhong, J. Zhang, X. Zhang, S. Lu and X.-j. Wang, *Appl. Phys. Lett.*, 2006, **88**, 201916.
20 Y. Jin, Y. Hu, L. Yuan, L. Chen, H. Wu, G. Ju, H. Duan and Z. Mu, *J. Mater. Chem. C*, 2016, **4**, 6614–6625.
21 M. Back, E. Trave, J. Ueda and S. Tanabe, *Chem. Mater.*, 2016, **28**, 8347–8356.
22 D. Chen, Y. Zhou, W. Xu, J. Zhong and P. Huang, *J. Mater. Chem. C*, 2016, **4**, 11457–11464.
23 N. Basavaraju, K. R. Priolkar, D. Gourier, S. K. Sharma, A. Bessière and B. Viana, *Phys. Chem. Chem. Phys.*, 2015, **17**, 1790–1799.
24 R. Zhong, J. Zhang, X. Zhang, S. Lu and X.-j. Wang, *Appl. Phys. Lett.*, 2006, **88**, 201916.
25 C. Walsh, J. Donegan, T. Glynn, G. Morgan, G. Imbusch and J. Remeika, *J. Lumin.*, 1988, **40**, 103–104.
26 W. Mikenda and A. Preisinger, *J. Lumin.*, 1981, **26**, 67–83.
27 W. Mikenda and A. Preisinger, *J. Lumin.*, 1981, **26**, 53–66.
28 M. Reynolds, W. Hagston and G. Garlick, *Phys. Status Solidi*, 1968, **30**, 113–117.
29 L. Li, Y. Wang, H. Huang, H. Li and H. Zhao, *Mod. Phys. Lett. B*, 2016, **30**, 1650019.
30 A. l. Bessieère, S. K. Sharma, N. Basavaraju, K. R. Priolkar, L. Binet, B. Viana, A. J. Bos, T. Maldiney, C. Richard and D. Scherman, *Chem. Mater.*, 2014, **26**, 1365–1373.
31 A. Bessière, S. Jacquart, K. Priolkar, A. Lecointre, B. Viana and D. Gourier, *Opt. Express*, 2011, **19**, 10131–10137.
32 F. Liu, Y. Chen, Y. Liang and Z. Pan, *Opt. Lett.*, 2016, **41**, 954–957.
33 Z. Pan, Y.-Y. Lu and F. Liu, *Nat. Mater.*, 2012, **11**, 58.
34 Z. Gong, Y. Liu, J. Yang, D. Yan, H. Zhu, C. Liu, C. Xu and H. Zhang, *Phys. Chem. Chem. Phys.*, 2017, **19**, 24513.
35 N. Basavaraju, K. R. Priolkar, A. Bessière, S. K. Sharma, D. Gourier, L. Binet, B. Viana and S. Emura, *Phys. Chem. Chem. Phys.*, 2017, **19**, 1369–1377.
36 A. De Vos, K. Lejaeghere, D. E. P. Vanpoucke, J. J. Joos, P. F. Smet and K. Hemelsoet, *Inorg. Chem.*, 2016, **55**, 2402–2412.
37 N. Basavaraju, K. R. Priolkar, D. Gourier, A. Bessière and B. Viana, *Phys. Chem. Chem. Phys.*, 2015, **17**, 10993–10999.
38 M. Allix, S. Chenu, E. Véron, T. Poumeyrol, E. A. Kouadri-Boudjelthia, S. Alahraché, F. Porcher, D. Massiot and F. Fayon, *Chem. Mater.*, 2013, **25**, 1600–1606.
39 D. Chen, Z. Wan, Y. Zhou and Z. Ji, *J. Eur. Ceram. Soc.*, 2015, **35**, 4211–4216.
40 J. Yang, Y. Liu, D. Yan, H. Zhu, C. Liu, C. Xu, L. Ma and X. Wang, *Dalton Trans.*, 2016, **45**, 1364–1372.
41 G. G. P. Van Gorkom, J. H. Haanstra and H. v. d. Boom, *J. Raman Spectrosc.*, 1973, **1**, 513–519.
42 G. Van Gorkom and J. Haanstra, *J. Raman Spectrosc.*, 1973, **1**, 513–519.
43 Y. Hemberger, N. Wichtner, C. Berthold and K. G. Nickel, *Int. J. Appl. Ceram. Technol.*, 2016, **13**, 116–124.
44 D. Gourier, A. Bessière, S. K. Sharma, L. Binet, B. Viana, N. Basavaraju and K. R. Priolkar, *J. Phys. Chem. Solids*, 2014, **75**, 826–837.
45 D. Chen, Z. Wan and Y. Zhou, *Opt. Lett.*, 2015, **40**, 3607–3610.
46 D. Chen, Y. Chen, H. Lu and Z. Ji, *Inorg. Chem.*, 2014, **53**, 8638–8645.
47 F. Castelli and L. S. Forster, *Phys. Rev. B*, 1975, **11**, 920.
48 D. Chen, X. Chen, X. Li, H. Guo, S. Liu and X. Li, *Opt. Lett.*, 2017, **42**, 4950–4953.
49 M. Hermus, P.-C. Phan, A. C. Duke and J. Brgoch, *Chem. Mater.*, 2017, **29**, 5267–5275.
50 R. Zou, S. Gong, J. Shi, J. Jiao, K.-L. Wong, H. Zhang, J. Wang and Q. Su, *Chem. Mater.*, 2017, **29**, 3938–3946.
51 V. B. R. Boppana and R. F. Lobo, *ACS Catal.*, 2011, **1**, 923–928.
52 Y. Li, S. Zhou, Y. Li, K. Sharafudeen, Z. Ma, G. Dong, M. Peng and J. Qiu, *J. Mater. Chem. C*, 2014, **2**, 2657–2663.
53 A. Ambast and S. Sharma, *Opt. Quantum Electron.*, 2017, **49**, 58.
54 J. T. Titantah and D. Lamoen, *Diamond Relat. Mater.*, 2007, **16**, 581–588.
55 M. Zhang, Y. Liu, H. Zhu, D. Yan, J. Yang, X. Zhang, C. Liu and C. Xu, *Phys. Chem. Chem. Phys.*, 2016, **18**, 18697–18704.
56 Y.-J. Li and X.-P. Yan, *Nanoscale*, 2016, **8**, 14965–14970.
57 P. Vijayaraghavan, C.-H. Liu, R. Vankayala, C.-S. Chiang and K. C. Hwang, *Adv. Mater.*, 2014, **26**, 6689–6695.
58 Q. Tian, M. Tang, Y. Sun, R. Zou, Z. Chen, M. Zhu, S. Yang, J. Wang, J. Wang and J. Hu, *Adv. Mater.*, 2011, **23**, 3542–3547.